NeuroImage 182 (2018) 314–328

Contents lists available at ScienceDirect

NeuroImage

journal homepage: www.elsevier.com/locate/neuroimage

Low frequency oscillating gradient spin-echo sequences improve sensitivity to axon diameter: An experimental study in viable nerve tissue

Lebina S. Kakkar [a,*,1], Oscar F. Bennett [a,1], Bernard Siow [b], Simon Richardson [b], Andrada Ianuş [a], Tom Quick [c], David Atkinson [d], James B. Phillips [e], Ivana Drobnjak [a]

[a] Centre for Medical Image Computing and Dept of Computer Science, University College London, London, UK
[b] Centre for Advanced Biomedical Imaging, University College London, London, UK
[c] Royal National Orthopaedic Hospital, Brockley Hill, Stanmore, London, UK
[d] Centre for Medical Imaging, Wolfson House, 4 Stephenson Way, London, UK
[e] Biomaterials and Tissue Engineering, UCL Eastman Dental Institute, 256 Grays Inn Road, London, UK

ARTICLE INFO

Keywords:
Diffusion imaging
Axon diameter
Oscillating gradient spin echo
Pulsed gradient spin echo
Single diffusion encoding
Viable tissue

ABSTRACT

Mapping axon diameters within the central and peripheral nervous system could play an important role in our understanding of nerve pathways, and help diagnose and monitor an array of neurological disorders. Numerous diffusion MRI methods have been proposed for imaging axon diameters, most of which use conventional single diffusion encoding (SDE) spin echo sequences. However, a growing number of studies show that oscillating gradient spin echo (OGSE) sequences can provide additional advantages over conventional SDE sequences. Recent theoretical results suggest that this is especially the case in realistic scenarios, such as when fibres have unknown or dispersed orientation. In the present study, we adopt the ActiveAx approach to experimentally investigate the extent of these advantages by comparing the performances of SDE and trapezoidal OGSE in viable nerve tissue. We optimise SDE and OGSE ActiveAx protocols for a rat peripheral nerve tissue and test their performance using Monte Carlo simulations and a 800 mT/m gradient strength pre-clinical imaging experiment. The imaging experiment uses excised sciatic nerve from a rat's leg placed in a MRI compatible viable isolated tissue (VIT) maintenance chamber, which keeps the tissue in a viable physiological state that preserves the structural complexity of the nerve and enables lengthy scan times. We compare model estimates to histology, which we perform on the nerve post scanning. Optimisation produces a three-shell SDE and OGSE ActiveAx protocol, with the OGSE protocol consisting of one SDE sequence and two low-frequency oscillating gradient waveform sequences. Both simulation and imaging results show that the OGSE ActiveAx estimates of the axon diameter index have a higher accuracy and a higher precision compared to those from SDE. Histology estimates of the axon diameter index in our nerve tissue samples are 4–5.8 μm and these are excellently matched with the OGSE estimates 4.2–6.5 μm, while SDE overestimates at 5.2–8 μm for the same sample. We found OGSE estimates to be more precise with on average a 0.5 μm standard deviation compared to the SDE estimates which have a 2 μm standard deviation. When testing the robustness of the estimates when the number of the diffusion gradient directions reduces, we found that both OGSE and SDE estimates are affected, however OGSE is more robust to these changes than the SDE. Overall, these results suggest, quantitatively and in *in vivo* conditions, that low-frequency OGSE sequences may provide improved accuracy of axon diameter mapping compared to standard SDE sequences.

1. Introduction

Developing a reliable technique to measure axon diameter *in vivo* is of great interest for our understanding of the human nervous system in both health and disease. Axon diameter has a direct effect on the speed of neural communication (Hursh, 1939; Ritchie, 1982) and hence varies in different regions of the central and peripheral nervous system. Larger axons are found in neural pathways that require rapid signalling, such as

* Corresponding author. Centre for Medical Image Computing (CMIC), University College London (UCL), Gower Street, London WC1E 6BT, UK.
E-mail address: lebina.shrestha.11@ucl.ac.uk (L.S. Kakkar).
[1] These authors contributed equally to this work.

http://dx.doi.org/10.1016/j.neuroimage.2017.07.060
Received 5 January 2017; Received in revised form 27 July 2017; Accepted 28 July 2017
Available online 1 August 2017

in the motor pathways of the peripheral and central nervous system. Smaller axons are located in pathways that allow slower neuronal communication such as those responsible for temperature and nociceptive sensations (Burke, 2007). Importantly, axon sizes, if found to be abnormal, can indicate the presence of certain neurological diseases. For instance, the presence of swollen axons in the lumbar spinal cord has been linked to amyotrophic lateral sclerosis, a degenerative disease of the central nervous system with an insidious onset (Sasaki and Maruyama, 1992; Cluskey and Ramsden, 2001). The axon diameters in controls and patients in Sasaki and Maruyama (1992) were shown to be 2.44 ± 0.51 μm and 3.32 ± 1.28 μm respectively, which suggests that controls and patients would be distinguishable by a method that could resolve a difference of a mean axon diameter of 0.88 μm or less. In autism, a higher density of unusually small axons in the anterior cingulate and orbitofrontal cortices has been associated with the mechanism responsible for the abnormalities in emotion and attention seen in the disorder (Piven et al., 1997; Zikopoulos and Barbas, 2010). Several peripheral nerve studies (Ikeda and Oka, 2012; Sanders, 1948) also suggest that axon diameter is a good indicator of the nerve regeneration rate. Hence, measuring axon diameter *in vivo* can be of great importance for a wide range of applications.

Numerous axon diameter imaging methods using diffusion MRI have been investigated in the literature. Q-space imaging (Ong and Wehrli, 2010), AxCaliber (Assaf et al., 2008), ActiveAx (Alexander et al., 2010) and double diffusion encoding (DDEs) (Benjamini et al., 2016; Komlosh et al., 2011) are important examples that have been previously proposed. Most of these techniques use conventional single diffusion encoding (SDE) spin echo sequences (also known as pulsed gradient spin echo (PGSE)), or DDE sequences which have been shown to have similar sensitivity to SDE at low diffusion weighting (Jespersen, 2012). However, various authors suggest that oscillating gradient spin-echo (OGSE) sequences should provide a number of important advantages over the more conventional SDE sequences in the context of axon diameter imaging (Drobnjak et al., 2016; Jiang et al., 2016; Mercredi et al., 2016; Parsons et al., 2006; Shemesh et al., 2015; Siow et al., 2012; Xu et al., 2014).

A common argument is that high-frequency OGSE sequences provide shorter effective diffusion time than SDE and hence are able to probe smaller length scales. This is clearly an advantage for measuring the free diffusivity in porous systems with small diameters because it minimizes the effects of restriction (Callaghan, 2011) and for measurements of surface to volume ratio (Reynaud et al., 2016). However, it is not clear whether it is advantageous for measuring axon diameter where contrast at longer diffusion times may be more informative.

Recently, a thorough numerical approach has been used to compare directly the sensitivity to axon diameter of SDE and OGSE sequences in a wide space of clinically plausible sequence parameters with trapezoidal diffusion gradient waveforms (Drobnjak et al., 2016). Signal sensitivity was measured as a derivative of the signal with respect to axon diameter and both parallel and dispersed fibre cases investigated. The research showed that, for the simple case of gradients perfectly perpendicular to straight parallel fibres, SDE always gives maximum sensitivity. However, in real-world scenarios where fibres have unknown and dispersed orientation, low-frequency OGSE provides higher sensitivity. This happens because the oscillating waveforms can achieve high sensitivity to axon diameters at a modest b-value, which in turn enables OGSE sequences to retain their sensitivity for unknown fibre orientations and in the presence of dispersion by avoiding excessive signal attenuation from unrestricted displacements in the fibre direction. Similar results were obtained for the axon diameter resolution limit for a range of different gradient strengths by Drobnjak et al. (2016) and confirmed analytically in Nilsson et al. (2017).

However, simulation experiments present idealised results and can never fully capture the varying complexities of tissues or the real environment of MR scanning. Even phantoms have been criticised for their simplicity and their inability to reflect the true microstructure in tissues (Burcaw et al., 2015; Li et al., 2014). In order to validate biophysical models and advanced diffusion sequences, it is necessary to test their predictions *in vivo* (Alexander et al., 2010; Santis et al., 2016). However, doing so can be hampered by an array of difficulties such as subject motion, restricted scan duration and invasive tissue extractions for histology. In order to avoid these issues a common compromise is to use fixated *ex vivo* tissue samples which allow imaging experiments to be continuously run for weeks if necessary (Dyrby et al., 2013; Xu et al., 2014). However, fixed tissue has low diffusivity and contains trapped water, both of which can contribute to changes in the diffusion signal leading to misleading parameter estimates that cannot be compared to those from *in vivo* samples. To bridge this gap between the *in vivo* state and the more convenient but less realistic fixed tissue experiments, Richardson et al. (2013) introduced the viable isolated tissue (VIT) system. This is an experimental technique that allows tissue samples to be kept in a physiologically stable state during which the nerve is as close to *in vivo* as possible, maintaining the same diffusion properties and experiencing negligible amount of degradation. The nerve can be kept in the VIT chamber for an extended period of time (≈ 12 h) and can therefore emulate *in vivo* imaging experiments with extensive acquisition times.

The purpose of this study is to experimentally test whether OGSE waveforms perform better than SDE waveforms when imaging axon microstructure in viable tissue, using the VIT system, with a direct comparison to histology. The study uses the ActiveAx framework to design and optimise the experiment and estimate tissue model parameters via a fitting process. ActiveAx is an orientationally invariant, experimental design optimisation algorithm (Alexander, 2008; Drobnjak et al., 2010), which selects diffusion measurement protocols that minimise the expected variance in the model parameters to be estimated. Originally this approach was constrained to SDE waveforms alone in the optimised protocols. Recently the approach has been extended to include the optimisation of the gradient waveform frequency, allowing the algorithm to select OGSE as well as SDE waveforms (Drobnjak and Alexander, 2011; Kakkar et al., 2017; Siow et al., 2013). In this study, we use OGSE and SDE ActiveAx and compare their performance first using Monte Carlo simulations and then on pre-clinical imaging data of a viable excised rat sciatic nerve. To compare the protocols, we evaluate them on three criteria: (i) Accuracy of the model estimates compared to the ground truth (for simulated data) or histology (for scanning data); (ii) Precision of the model estimates; (iii) Robustness of the model estimates as the total number of diffusion gradient directions reduces.

2. Methods

2.1. Tissue samples

A sample of sciatic nerve tissue, approximately 1 cm in length, is freshly excised from an adult Sprague Dawley rat. The nerve is carefully ligated using 4/0 silk sutures at both ends, which are further used to tie the nerve to a platform. The nerve-platform ensemble is then inserted into a specially designed viable isolated tissue (VIT) chamber as in Richardson et al. (2013), which bathes the tissue in a temperature controlled (at 37^{o}C) oxygenated artificial cerebrospinal fluid (aCSF) solution in order to preserve viability during the course of the image acquisition. Fig. 1 shows the nerve contained inside this chamber.

The experiments comply with the ARRIVE guidelines and are carried out in accordance with the U.K. Animals (Scientific Procedures) Act, 1986 and associated guidelines, EU Directive 2010/63/EU for animal experiments (Home Office, 2000).

2.2. Tissue model

We use a simplified version of the CHARMED model (Assaf and Basser, 2005; Assaf et al., 2004) to represent the nerve microstructure. This is a two compartment model made up of the following compartments:

- Intra-axonal compartment. Similar to Alexander et al. (2010), this compartment models the signal S_1 coming from within non-abutting

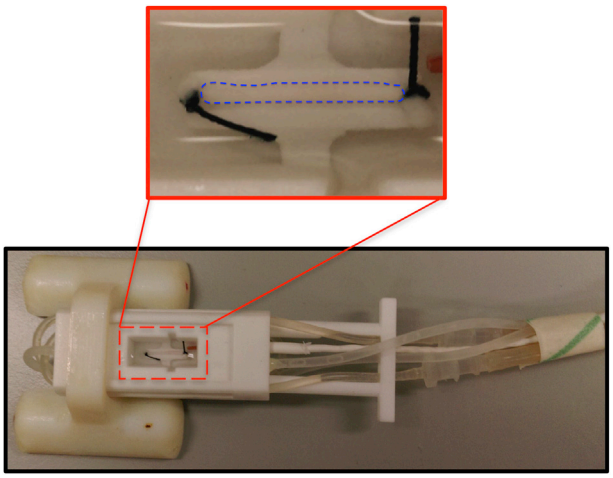

Fig. 1. The bottom image shows the chamber used to hold the excised and ligated nerve tissue within the bore of the scanner during the image acquisition. The top image displays the magnified sciatic nerve (outlined in blue dashed lines), which is ligated at both ends, and tied to a platform that is attached to the chamber via a couple of inserts. The full nerve sample, in reality, extends beyond the sutures. Details about the chamber can be found in Richardson et al. (2013).

parallel cylinders each with a single diameter a. We assume that the intra-axonal space is a perfect cylinder, and hence the diffusion in it can be characterised with intrinsic diffusivity, which we refer to here as $d_{||}$.

- Extra-axonal compartment. Similar to Alexander et al. (2010) and Drobnjak et al. (2016), this compartment models the signal S_2 using anisotropic Gaussian displacements (Basser et al., 1994). We assume unhindered diffusion along the axons and hence characterise it with intrinsic diffusivity $d_{||}$. Hindered diffusion perpendicular to the axons is characterised with the apparent diffusivity d_h. $d_{||}$ is the same in both intra- and extra-axonal compartment.

No exchange between the water populations of the two compartments is assumed because in myelinated sciatic nerves, the inter-compartment water exchange time is on the order of seconds (Dortch et al., 2013), which is much longer than the diffusion times in this study and has little influence on the measured signal (Nedjati-Gilani et al., 2017; Nilsson et al., 2013). Henceforth, the full model for the diffusion MRI signal, S, is:

$$S = S_0(fS_1 + (1-f)S_2) \tag{1}$$

where, S_0 is the non-diffusion weighted signal and f corresponds to the volume fraction of water within the intra-axonal compartment.

2.3. Protocol optimisation and imaging protocol

The OGSE and SDE diffusion imaging protocols are both optimised for the peripheral nerve tissue model using the optimisation framework from Alexander (2008) and Drobnjak et al. (2010). The optimisation seeks the diffusion sequence parameters: gradient strength (G), diffusion time (Δ), gradient duration (δ) and also, in the case of OGSE, the waveform frequency (ω); that maximise sensitivity to the tissue model parameters. The optimisation minimizes the mean Cramer-Rao Lower Bound (CRLB), which provides a lower bound on the variance of a fitted tissue model parameter that usually correlates closely with the true variance. We assume a Rician noise model; the full expression for the CRLB assuming the Rician noise is in Alexander (2008). OGSE sequences are implemented with the same gradient waveform before and after the RF 180° pulse. Previous simulations (not shown) found no significant difference in the waveform shapes output by the optimisation if the gradient polarity is reversed after the RF 180° pulse.

Both OGSE and SDE protocols are optimised using *a priori* model parameters settings of $f = 0.60$ (obtained from Kempton et al. (2009)), $d_{||} = 1.7\ \mu m^2/ms$ (obtained from Alexander et al. (2010)), $d_h = 0.68\ \mu m^2/ms$ (assumes tortuosity constraint (Szafer et al., 1995)) and axon diameter indices of 2.26, 4.50, and 6.74 μm (obtained from Ikeda and Oka (2012)). We optimise three protocols independently from one another, each protocol with a different number of gradient directions $N \in \{8, 16, 32\}$ per shell, in order to quantify the robustness of estimating axon diameter as the number of directions reduces. Gradient directions are uniformly sampled on the sphere (Alexander, 2008) and fixed for each protocol. Each protocol has three HARDI shells for which the shape and the parameters of the gradient waveforms (and implicitly the b-value), are optimised using the following scanner settings $G_{max} = 800$ mT/m, slew rate = 2000 T/m/s and maximum echo time (TE) = 40 ms. The gradient waveform shape in the OGSE protocol is constrained to sine-like trapezoidal waveforms. The final optimised protocols for SDE and OGSE, for the three separate gradient directions sets (8, 16 and 32), are displayed in Fig. 2, each with 3 HARDI shells and unique b-values. An additional 9 b = 0 images (non-diffusion weighted measurements) are also included in the final optimised protocols to allow estimation of the noise variance per voxel, which is required later for model fitting.

All MR measurements are conducted with a small bore 9.4T scanner (Agilent Inc., Santa Clara, CA, USA) equipped with 1000 mT/m imaging gradients and a 33 mm RF bird cage volume coil (RAPID, Biomedical GmbH, Rimbar, Germany). A single-slice fast spin-echo readout is used with an echo train length of 8, where the slice is chosen to be at the middle of the platform (i.e. the location of the 'inserts'). The following imaging parameters were used: FOV = 6 mm × 6 mm × 2 mm, matrix size = 64 × 64, voxel dimensions = 93.8 μm × 93.8 μm × 2 mm, 8 signal averages, TR = 1100 ms, effective TE (SDE) = 20 ms and effective TE (OGSE) = 35 ms. The total time necessary to complete all imaging protocols is approximately 12 h. In order to remove cross-terms created by the crusher and imaging gradients (Mattiello et al., 1994), the diffusion gradients are calibrated in a post processing step using phantom plates in a similar manner to Kakkar et al. (2017). The results from the calibration are summarised in Supplementary Material 1.

2.4. Simulation substrates

We use Monte-Carlo diffusion simulations via the CAMINO framework (Alexander, 2008; Cook et al., 2006; Hall and Alexander, 2009) and generate synthesised data using 3-D digital phantoms representing the nerve tissue substrates. Each phantom is characterised as a unique combination of four parameters: the shape k and the scale parameter θ of the axon radius distribution, the intrinsic diffusivity of spins $d_{||}$, and the intra-axonal volume fraction f, where Best's algorithm (Devroye, 1986) is used to ensure proper sampling of the diameter distribution. To mimic the structure of the rat peripheral nerve, we model the nerve as a collection of non-abutting parallel cylinders with radius drawn from a gamma distribution.

The shape and the scale parameters of the gamma distribution are determined from a collective fibre radius histogram of normal rats shown in Ikeda and Oka (2012), which are further corrected to axon radius using g-ratio values reported there. We construct twenty-eight unique nerve substrates, with substrate parameters: $(k,\theta) \in \{(4.08, 4.58 \times 10^{-7}), (7.49, 2.27 \times 10^{-7}), (4.08, 3.27 \times 10^{-7}), (7.49, 1.86 \times 10^{-7}), (7.49, 1.65 \times 10^{-7}), (7.49, 1.45 \times 10^{-7}), (7.49, 1.03 \times 10^{-7})\}$; $f \in \{0.4, 0.5, 0.6, 0.7\}$ and $d_{||} = 1.7\ \mu m^2/ms$. The cylinders are randomly packed in the substrates as described in Hall and Alexander (2009), with example substrates shown in Fig. 3. Distribution of cylinder diameters for each substrates is described using a single summary statistic α, which we call the "axon diameter index", as in Alexander et al. (2010), and is described using the following equation:

$$\alpha = \frac{\sum_{i=1}^{n} a_i^3}{\sum_{i=1}^{n} a_i^2} \tag{2}$$

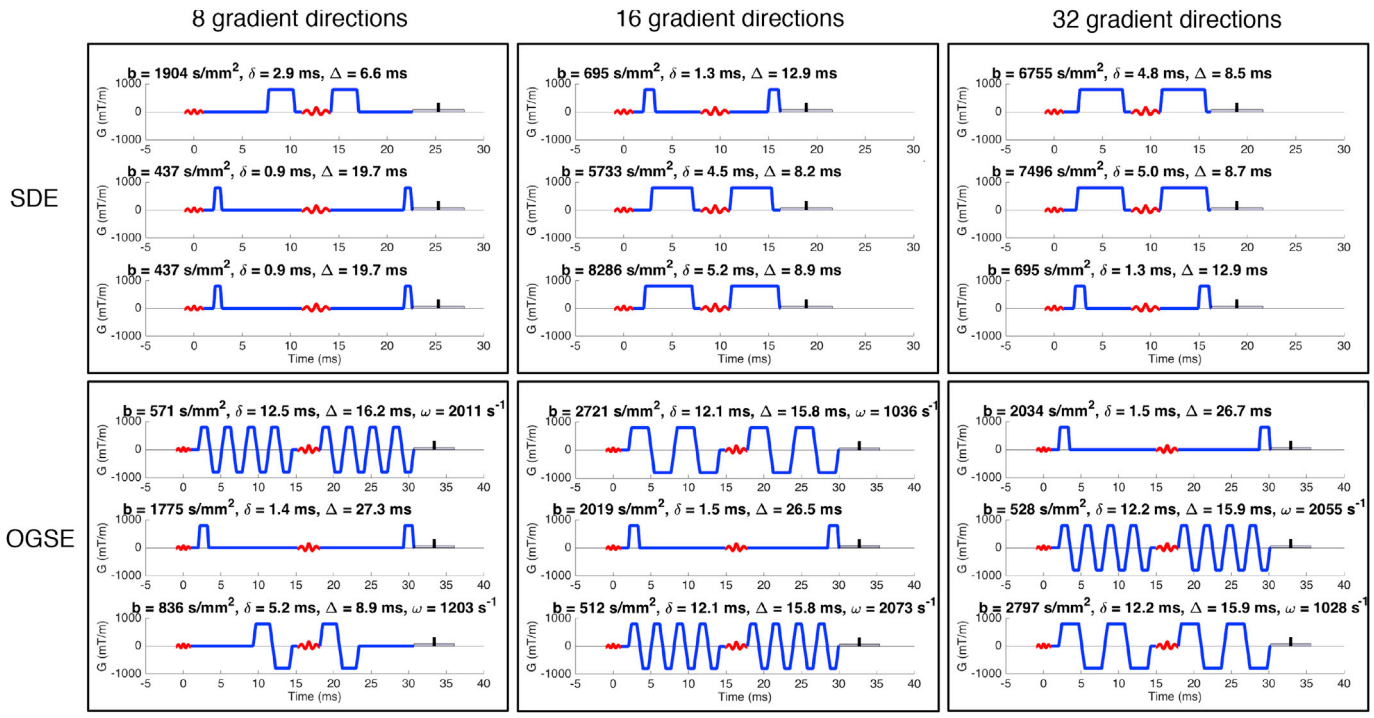

Fig. 2. The optimised protocols for SDE (top row) and OGSE (bottom row). Each protocol contains three shells which have the same number of gradient directions: 8 for the protocol in the left column, 16 for the protocol in the middle column and 32 for the protocol in the right column. Red markers indicate RF pulses and the blue lobes indicate diffusion encoding magnetic field gradients. The sequence parameters are also given for each measurement as: b-value (b), duration of the first gradient waveform (δ), time between the start of the first gradient waveform and start of the second gradient waveform (Δ) and frequency of the waveforms (ω)(for oscillating waveforms). Note that the order of the shells is arbitrary.

where n is the number of cylinders, and a_i are the diameters sampled from the distribution of a given substrate.

The simulations are based on the inner axon diameter values and myelin areas are not included. All simulations are performed using 200000 spins, 6000 time steps and 500 cylinders. We chose these values as they provide precision of 10^{-10} of the unweighted signal, which is several orders of magnitude smaller than realistic signal noise (Hall and Alexander, 2009). In order to make the synthesised dataset more realistic, 50 different instances of random Rician noise (SNR = 10) are introduced to the final dataset.

2.5. Model fitting

An adapted voxel-wise model fitting procedure described by Alexander et al. (2010) is used to estimate f, $d_{||}$, d_h and a. Since the model assumes a single diameter, in a substrate with multi-diameter cylinders where the signal contribution of each cylinder is proportional to the amount of water it contains, a reflects the volume weighted average diameter we introduced in Equation (2). Hence, throughout the manuscript we will refer to this single fitted diameter as axon diameter index α as in Alexander et al. (2010).

In the fitting procedure first, in order to reduce the number of combinations of parameters which helps with model stability, a diffusion tensor is fitted to the data to find the fibre orientation (Alexander et al., 2010). In the simulation case, d_h is estimated assuming all other parameters are fixed to the ground truth values and d_h is constrained to be smaller than $d_{||}$. Then, a two stage fitting process that involves a grid search, and then a gradient descent algorithm is performed to estimate f,

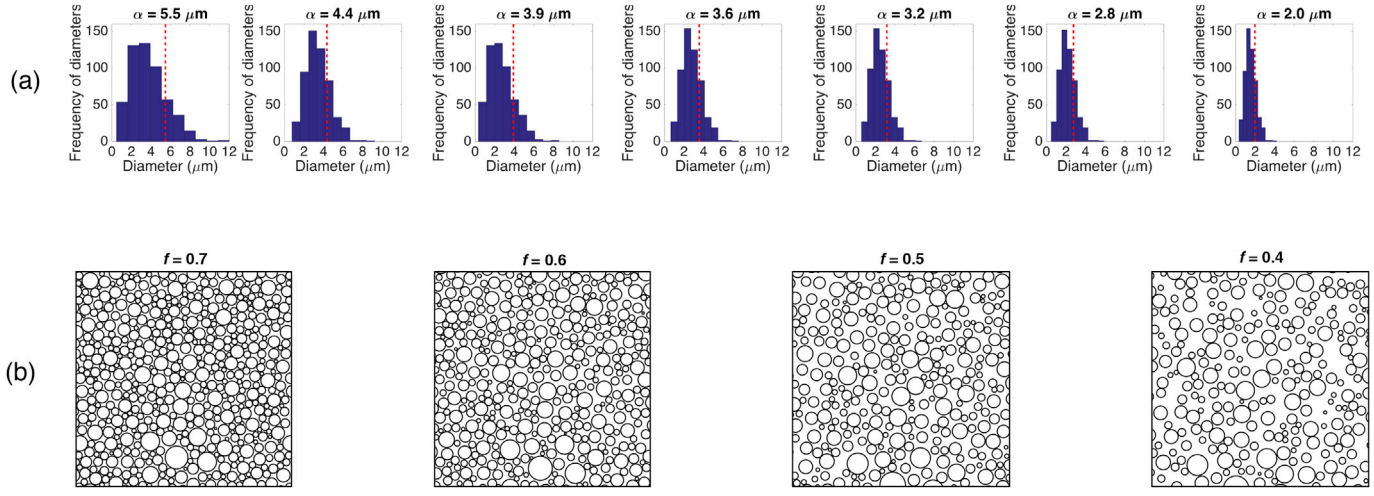

Fig. 3. (a) shows histograms of axon diameter distributions we use to generate digital substrates for the Monte Carlo simulations. The axon diameter index is calculated for each and shown as a red dashed line. (b) shows digital tissue substrates for the histogram furthest to the right in a) and four different intra-axonal volume fractions we use in simulations. In simulations, each histogram is combined with each of the four volume fractions producing twenty-eight different substrates.

$d_{||}$ and α using the calculated fibre orientation and the estimated d_h. In the tissue case, since the ground truth d_h is unknown, d_h is fixed to a range of values from 0.3 μm^2/ms (the minimum calculated d_h from simulations) to 3 μm^2/ms (the diffusivity of free water at 37°C (Holz et al., 2000)) with an interval of 0.01 μm^2/ms, and again constrained to be lower than $d_{||}$. For each fixed d_h the two step fitting procedure described previously is applied to estimate the rest of the parameters and the combination of all parameters that gives the maximum log likelihood is selected.

We then use the estimated parameters to test the accuracy and the robustness of the protocols. In order to test the precision of the estimates, we additionally run a Markov Chain Monte Carlo (MCMC) procedure assuming a Rician noise model. The gradient descent provides a starting point for the MCMC which then collects 125 samples at intervals of 30000 iterations after a burn in of 5000 iterations. We then calculate the standard deviation of the posterior distribution of the parameter estimates and use it to test the precision of the protocols.

2.6. ROI selection

In order to perform quantitative analyses of the results from model fitting a region of interest (ROI) fully within the nerve is selected (see Fig. 10). The region corresponds to the approximate extent of the large upper axon-rich nerve fascicle seen in the histology. Voxels from this region are least likely to contain partial volume of the axon-free epineurium or of free water outside the nerve and so are most suitable to use for assessment of the chosen tissue model. A preprocessing step in the analysis excludes a small subset of the ROI voxels from each protocol which have a signal-to-noise ratio (SNR) < 10 and a fractional anisotropy (FA) < 0.2.

2.7. Histology

The histology procedure is carried out as described in Richardson et al. (2013). The nerve tissue sample is removed from the chamber, still attached to the platform, and fixed in 2% paraformaldehyde, 2% glutaraldehyde and sodium cacodylate buffer (pH 7.3). The sample is post-fixed with 1% osmium tetraoxide, dehydrated, set in resin, sectioned and then stained with lead citrate in preparation for transmission electron microscopy. The tissue section is extracted and then imaged with a Joel 1010 transmission electron microscope and the images recorded using a Gatan Orius CCD camera. Throughout imaging, fixation and tissue sample extraction, the nerve is kept on a platform that has inserts crossing the middle region (top of Fig. 1). These inserts are used for slice localisation during MR imaging and also during the tissue section extraction in order to match the histology sample with the MR imaging slice.

Thirty 64 × 50 × 5 μm transmission electron micrographs (TEM), an example is shown in Fig. 4, obtained at regularly spaced positions across the whole nerve section are acquired to sample the axon microstructure. An in-house MATLAB (The MathWorks, Natick MA.) based image processing algorithm is used to automatically extract the size and number of intra-axonal areas in each image. The algorithm involves a threshold segmentation of the axon myelin sheaths, followed by morphological operations to clean up the resulting segmentations, and then finally a connected component analysis that extracts the intra-axonal regions from within the images. Results are checked visually to ensure accurate segmentation before further analysis takes place.

These intra-axonal regions are then used to calculate the local intra-axonal volume fraction and the local axon diameter index. The local intra-axonal volume fraction is calculated by dividing the total area of all the intra-axonal regions with the total area in the image (excluding the myelin sheath). The effective diameters come from the intra-axonal regions not connected to the image edges. These diameters are calculated by taking the cross sectional area of each axon and then calculating the diameter of a cylinder that would have such a cross sectional area.

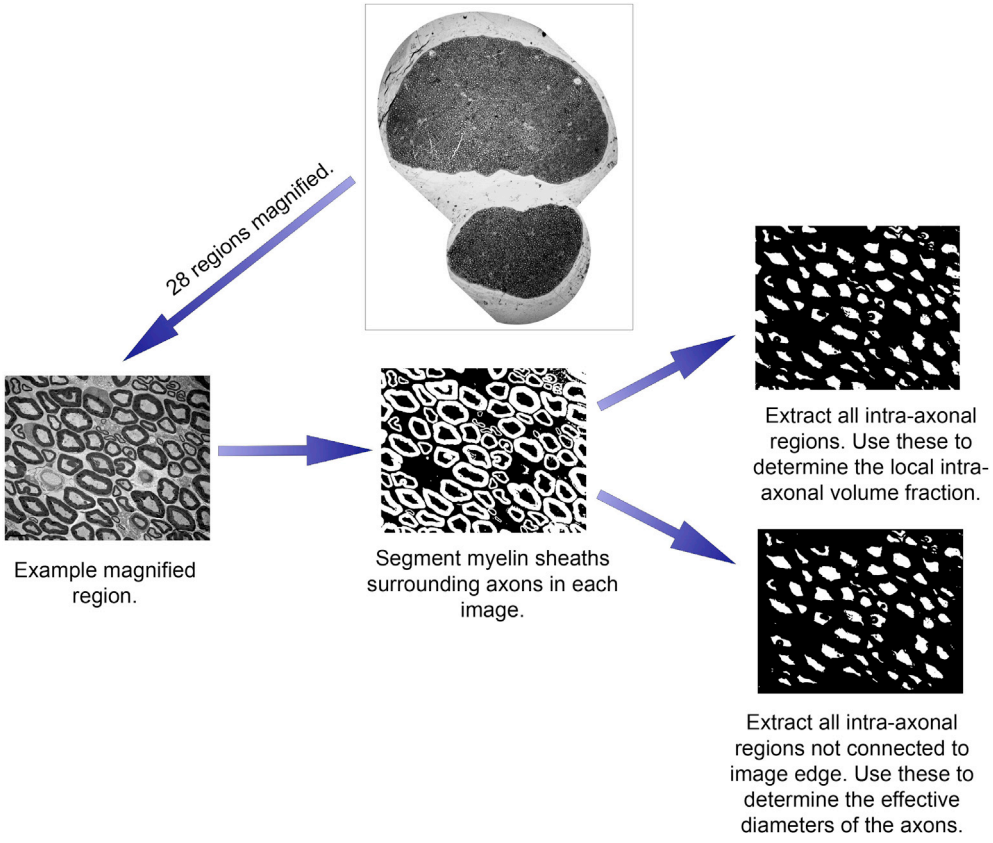

Fig. 4. An outline of the main steps in the image processing algorithm implemented for histological microstructure measurements. Minor intermediate steps in the pipeline have been omitted.

Additionally these effective diameters are corrected for tissue shrinkage of 30% as suggested by Innocenti et al. (2014a). The local axon diameter index (computed using Equation (2)) and local intra-axonal volume fraction for each TEM image are used for comparison with the parameter estimates obtained from model fitting. An outline of the TEM processing pipeline is shown in Fig. 4.

3. Results

3.1. Simulation experiments

Fig. 5 shows the fitted model signal for two example substrates for 32 direction SDE and OGSE protocols. As expected, both protocols show that the substrate with the small diameter index ($\alpha = 2.78\ \mu$m) shows lower attenuation than the substrate with the larger diameter index ($\alpha = 4.37\ \mu$m). The trend is more clearly shown using the corresponding noise free data of the substrates in Supplementary Material 2. Higher attenuation occurs for larger diameters because diffusion can occur for a longer time without coming across any boundaries. Green lines (marked with inverted triangles) seem to undershoot the data. This is an expected effect, which happens because the data contains Rician noise (which is always positive) and is mainly observed at large b-values in the parallel direction. During model fitting we account for Rician noise, hence the fitted curves are below the data points. To assess the model fit accuracy we plot simulated raw data with underlying ground truth parameters and without any noise (solid lines). The figure shows a good match between the ground truth simulated data (solid lines) and data predicted from the model fit (dashed lines). We tested the degree of agreement using a χ^2 test and found that across all the simulated substrates for SDE the median χ^2 is 0.18, and the interquartile range (0.06, 0.49), while for OGSE the median χ^2 is 0.12, and the interquartile range (0.05, 0.29), suggesting a slightly better agreement for the OGSE protocol.

Fig. 6 shows the SDE and OGSE estimated model parameters plotted against the ground truth diameter indices for the simulated cylinder substrates. The results are shown for the 32 gradient direction protocol. The first row shows that although SDE shows a positive correlation with the ground truth index, it overestimates the diameter index for almost all substrates while the OGSE protocol is much more accurate, with estimates closer to the ground truth. Both OGSE and SDE underestimate axon diameters for substrates with a large axon diameter index, which happens because the protocols are optimised for smaller diameters and hence their diffusion times are not long enough to probe large diameters. The intra-axonal volume fraction estimates in the second row are slightly underestimated for OGSE sequences and slightly overestimated for SDE sequences. In terms of diffusivities (third and fourth rows), both OGSE and SDE sequences perform similarly.

Fig. 7 displays the uncertainty in SDE and OGSE model parameter estimates across all substrates, intra-axonal volume fractions and across the 50 different instances of random Rician noise (SNR = 10). The uncertainty is represented by the standard deviation of the posterior distribution on the model parameter estimate. The uncertainties in the estimates of diameter index (first row), intra-axonal volume fraction (second row) and intrinsic diffusivity (third row) from the OGSE protocol are significantly lower than the SDE protocol with $p \approx 1 \times 10^{-27}$, which is calculated using a two-sided Wilcoxon rank sum test with a sample size of 1400. We get test statistics of $W = 2.6 \times 10^6$, $W = 2.5 \times 10^6$ and $W = 2.2 \times 10^6$, respectively, for the diameter index, intra-axonal volume fraction and intrinsic diffusivity, respectively. The uncertainty of hindered diffusivity is not calculated because it is fixed to a pre-calculated value (mentioned above) throughout the fitting procedure. In addition to this, Fig. 17 in Supplementary material 3 compares the performance of OGSE and SDE protocols shown separately for substrates with different

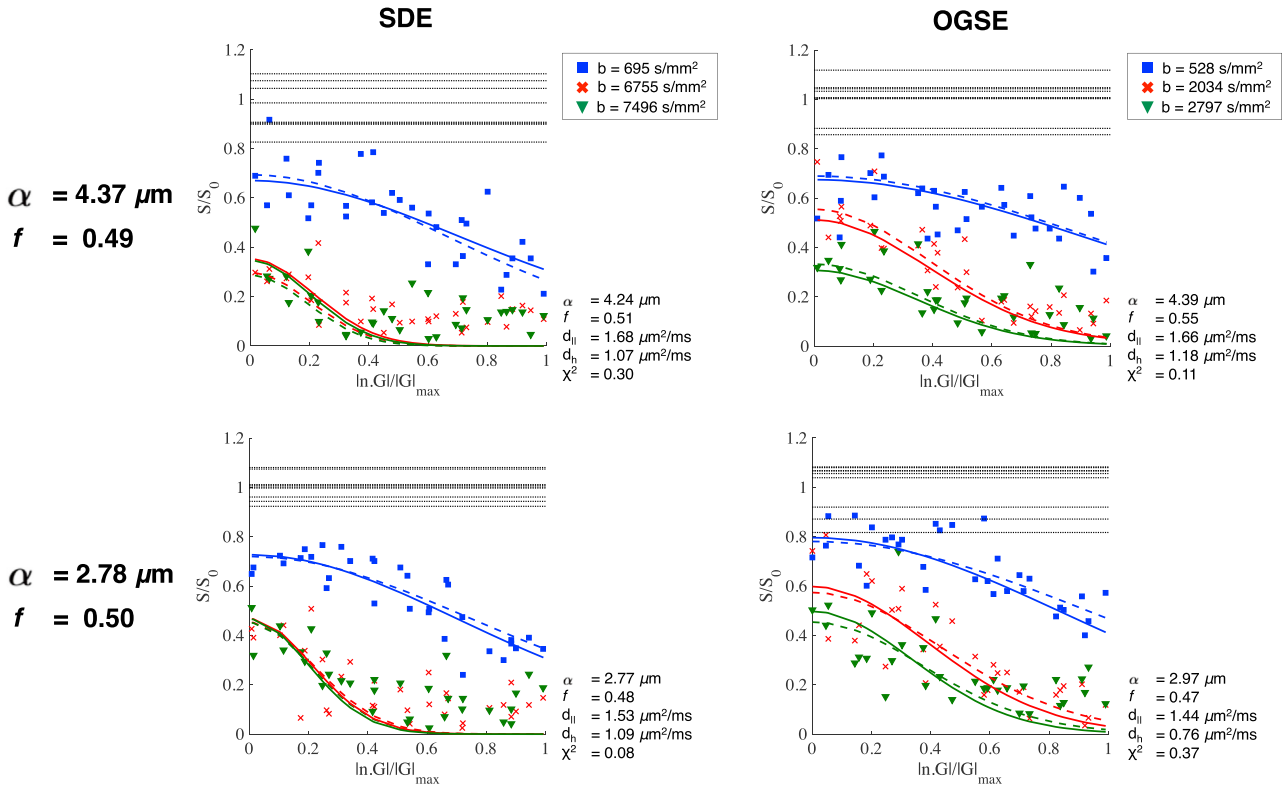

Fig. 5. Figure shows simulated data with SNR = 10 (data points), predicted signal using estimated model parameters (dashed lines) and simulated signal using ground truth model parameters (solid lines) for two example substrates from the 32 gradient directions SDE (left column) and OGSE (right column) protocols. The horizontal axis is the absolute dot product between the gradient directions and the estimated fibre orientation. The estimated parameters are shown in the bottom right hand corner of each graph, along with the χ^2 value to indicate the agreement between the fitted signal and the simulated signal calculated using the ground truth model parameters. The horizontal dashed lines around $S/S_0 = 1$ represent the 9 non-diffusion weighted measurements and their variation corresponds to the added Rician noise in the data.

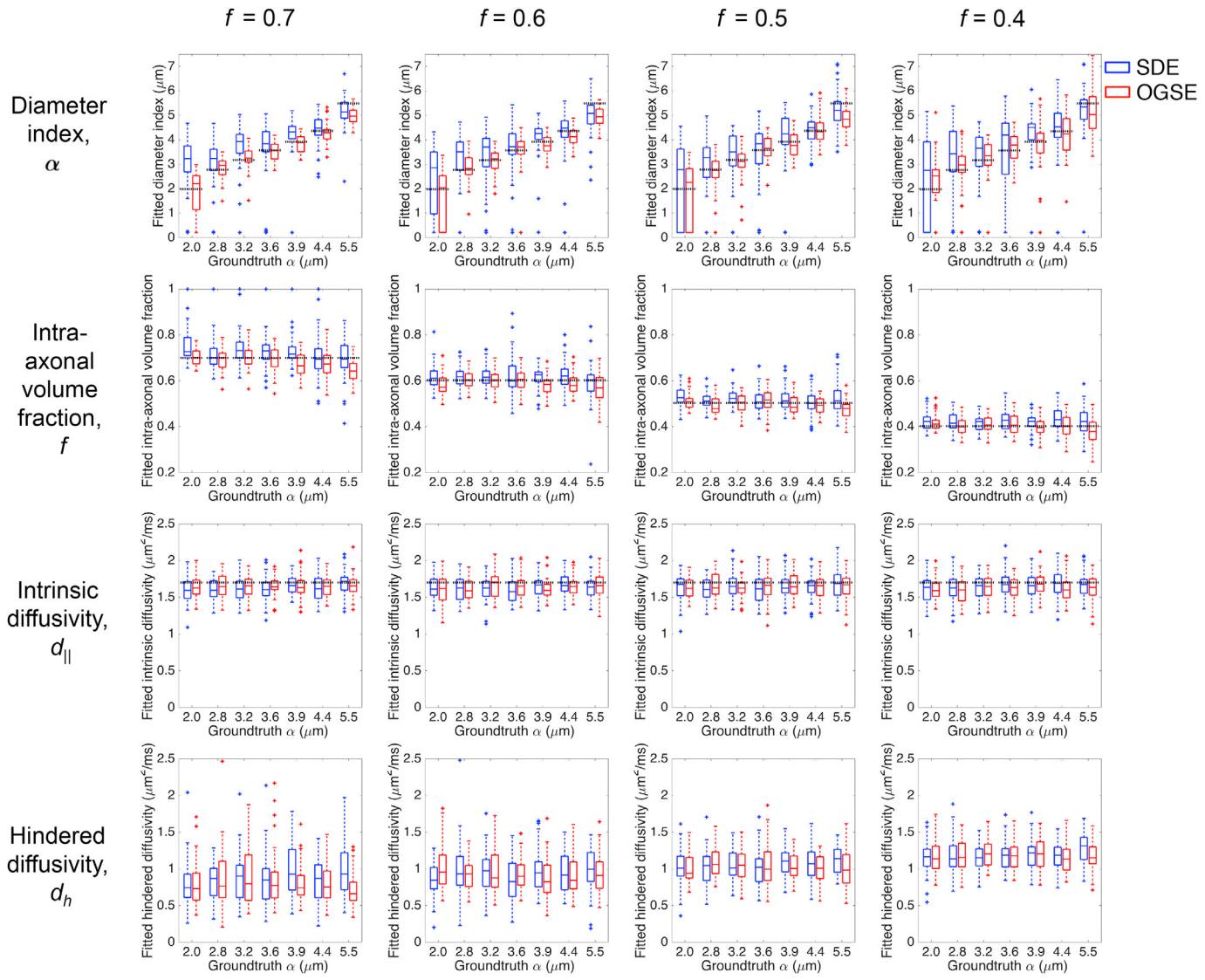

Fig. 6. Accuracy of estimated model parameters in simulation experiments: axon diameter index (1st row), intra-axonal volume fraction (2nd row), intrinsic diffusivity (3rd row) and hindered diffusivity (4th row) for a range of intra-axonal volume fractions. The box-whisker plots of the model parameter estimates, across 50 different instances of random Rician noise (SNR = 10), are shown for each diameter index, with SDE in blue (left) and OGSE in red (right). The boxes show median, 25th and 75th percentiles of the uncertainty and the whiskers extend to the most extreme data points excluding outliers. The ground truth parameters of the substrates are shown as dashed black lines. d_h plots do not have any black lines as the ground truth for d_h is unknown and depends on the packing.

diameters and volume fractions. We find that diameter estimates have slightly larger uncertainties for smaller diameters, and that these increase as the volume fraction decreases. For volume fraction the trend is reversed. Across all diameters and volume fractions we find SDE to have much larger (statistically significant) uncertainties compared to OGSE, similar to Fig. 7. Overall, the OGSE appears to estimate parameters with higher precision across the range of substrates compared to SDE.

Fig. 8 compares the robustness of parameter estimates between SDE and OGSE protocols across the number of measurement directions (shown in columns) for the full range of synthetic substrates. The box and whisker plots on each graph represent the range of median estimates for each substrates across its 50 instances of added noise. OGSE protocols consistently deliver estimates of diameter indices that are within the ground truth range regardless of the number of gradient directions used. This is clearly seen to be the case for the majority of substrates in Fig. 18 (Supplementary material 3) in which substrates with different diameters are separately plotted. In addition to high accuracy, OGSE estimates also have a lower interquartile range with respect to the noise and these ranges are consistent in size across most measurement directions. SDE estimates of diameter indices reduce in accuracy and robustness to noise as the number of directions reduces. In terms of the intra-axonal volume fraction and diffusivities, both protocols show similar estimates across the three sets of gradient directions. Both protocols also show an expected increase in the number of outliers as the number of directions are reduced. Overall, OGSE seems to exhibit greater robustness for diameter indices as the number of diffusion measurements reduces compared to SDE estimates.

3.2. *Viable nerve tissue experiment*

3.2.1. *Histology results*

Fig. 9 shows examples of micrographs obtained from the TEM procedure described in Section 2.7. The entire nerve section is shown with the upper and the lower fascicles where the axons are. The image of the nerve is created by composing two large scale TEM images, and has been rotated to coincide with the orientation of the nerve in the MR images and parameter maps presented later.

The ground truth microstructure measurements are obtained from twenty-eight of the thirty magnified regions (two of the TEM failed segmentation due to histology processing artefacts) using the image

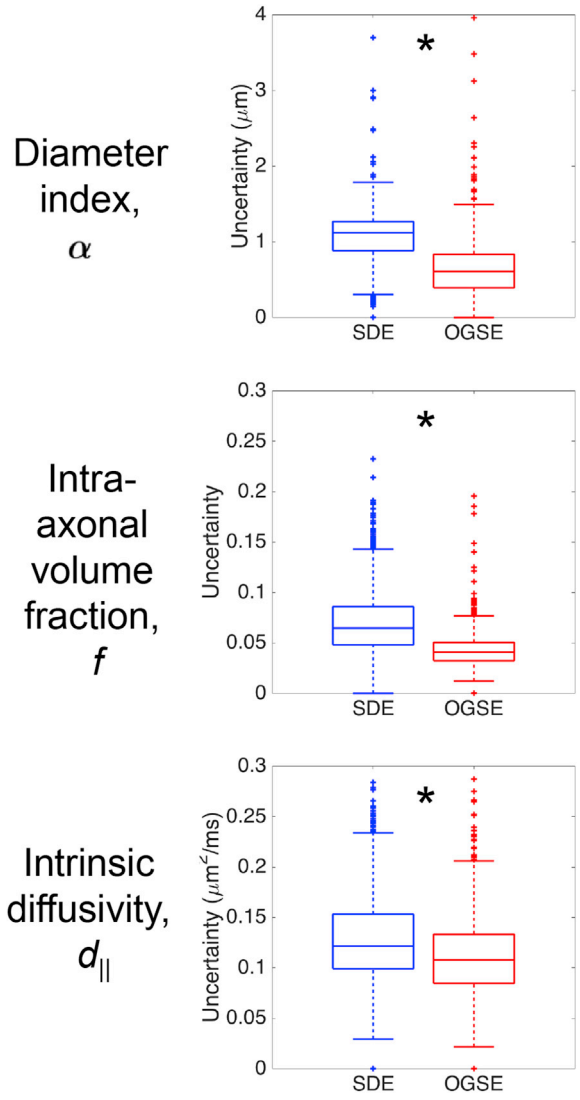

Fig. 7. Precision of estimated parameters in simulation experiments. Box-whisker plots of the standard deviation of the posterior distribution, i.e. uncertainty, on the estimated axon diameter index (1st row), intra-axonal volume fraction (2nd row) and intrinsic diffusivity (3rd row) for all substrates across all intra-axonal volume fractions and across 50 different instances of random Rician noise (SNR = 10). The 32 gradient direction SDE and OGSE values are shown in blue and red, respectively. The boxes show median, 25th and 75th percentiles of the uncertainty and the whiskers extend to the most extreme data points excluding outliers. The * represents significant differences ($p \approx 1 \times 10^{-27}$) in the uncertainties of the model parameter estimates from the SDE and OGSE protocols.

processing algorithm. Interestingly, the majority of the sample regions do not seem to exhibit a gamma distribution of axon diameters. After shrinkage correction, often the smallest axons (below 3 μm) are the most numerous (≈45% of the average sample) and the larger axons (>5 μm) are fewer in numbers (≈13% of the average sample). Overall, the averaged local axon diameter index across the twenty-eight samples is 4.80 ± 0.58 μm. The averaged local intra-axonal volume fraction is 0.44 ± 0.11.

3.2.2. *Imaging results*

Fig. 10 shows: a) a T_2 weighted cross-sectional image of the nerve with no diffusion weighting applied; and b) the region of interest (ROI) used for model fitting. The red region covers the whole of the cross-sectional area of the nerve. The green region covers the inner area of the upper fascicle of the nerve seen in Fig. 9 to ensure no partial volume effects. We selected voxels at least one pixel away from the edge of the nerve and also ensured that only voxels with FA ≥ 0.2 and SNR ≥ 10 were chosen. Model fitting was performed on all voxels, however, only voxels from the green region were used for the quantitative analysis.

Fig. 11 shows a quality of fit for an example voxel in the green ROI of the nerve. Estimated model parameters are shown in the bottom right corner, the model predictions using those parameters are in dashed lines and the imaging data is marked with crosses. Similarly to the simulation results, the signal in the free diffusion direction (for $|\mathbf{n}.\mathbf{G}|/|\mathbf{G}_{max}| \rightarrow 1$) cannot be distinguished from the noise floor for b > 2000 s/mm^2. The model prediction visually shows a good fit with the measured data and this is further quantified with the Rician log likelihood (R_{log}) (Alexander, 2008) of the fitted signal given the measured data. A median R_{log} of 167 and an interquartile range (159, 172) are found for the SDE protocol while the OGSE protocol has a lower median R_{log} of 110 and an interquartile range (100, 119). Both are of the same order of magnitude as the expected R_{log} for an average SNR estimated from the data, suggesting a good fit.

Fig. 12 shows the diameter index and intra-axonal volume fraction maps computed from the 32 gradient direction protocols. The estimated parameter values on the right (blue crosses for the SDE and red squares for the OGSE) are from the green ROI shown in Fig. 10. The figure shows that the SDE protocol overestimates the axon diameter index compared to the histology based estimates (in black), while the OGSE protocol results are in excellent agreement with the histology. Both SDE and OGSE protocol estimates of intra-axonal volume fraction are aligned with histology, however OGSE estimates are more tightly within the histology range while some of the SDE voxels are outside of that range. Estimates of diffusivity (data not shown here) are aligned between the two protocols. These results suggest that the OGSE protocol outperforms the SDE protocol regarding the accuracy of the estimated parameters are in line with the simulation results in Fig. 6.

Fig. 13 quantifies the differences in the level of precision between the OGSE and SDE 32-direction protocol by using uncertainty values of the axon diameter index (top), intra-axonal volume fraction (middle) and intrinsic diffusivity (bottom) from the voxels within the green ROI in Fig. 10b. The uncertainties across diameter index and intra-axonal volume fraction estimates for the SDE protocol are higher than those from OGSE protocols, which although not statistically significant (using a two-sided Wilcoxon rank sum test), are in line with the simulation findings.

Fig. 14 quantitatively demonstrates how the parameter estimates from OGSE and SDE protocols are affected by a change in the number of measurement directions included in the protocol. Similar to the simulation results in Fig. 8, this figure suggests that changes in the number of measurements seem to affect the OGSE parameter estimates less than those of SDE as we move from 32 to 16 measurement directions. In the case of 8 measurement directions, the SDE protocol appears to have less variation in the diameter and intra-axonal volume fraction estimates compared to the OGSE protocol, however, the SDE protocol has higher hindered diffusivity than the estimates from more reliable protocols of 16 and 32 gradient directions. In the case of intrinsic diffusivity, OGSE and SDE protocols both provide robust estimates.

4. Discussion

In this work, we have compared the performance of the OGSE ActiveAx method with the standard SDE ActiveAx method by comparing their ability to estimate axon diameters in tissue. We show that the optimal OGSE protocol (consisting of one SDE sequence and two low frequency oscillating diffusion waveforms) consistently outperforms SDE in both simulated substrates and a viable rat sciatic nerve. The OGSE ActiveAx estimates of axon diameter have a higher accuracy and a higher precision compared to those from SDE. Furthermore, OGSE estimates are more robust compared to the SDE estimates when the number of measurements available for model fitting is reduced. Finally, the OGSE ActiveAx estimates of axon diameter and volume fraction are in remarkable agreement with histology results. These results suggest for the first time, quantitatively and in an as close as possible to *in vivo*

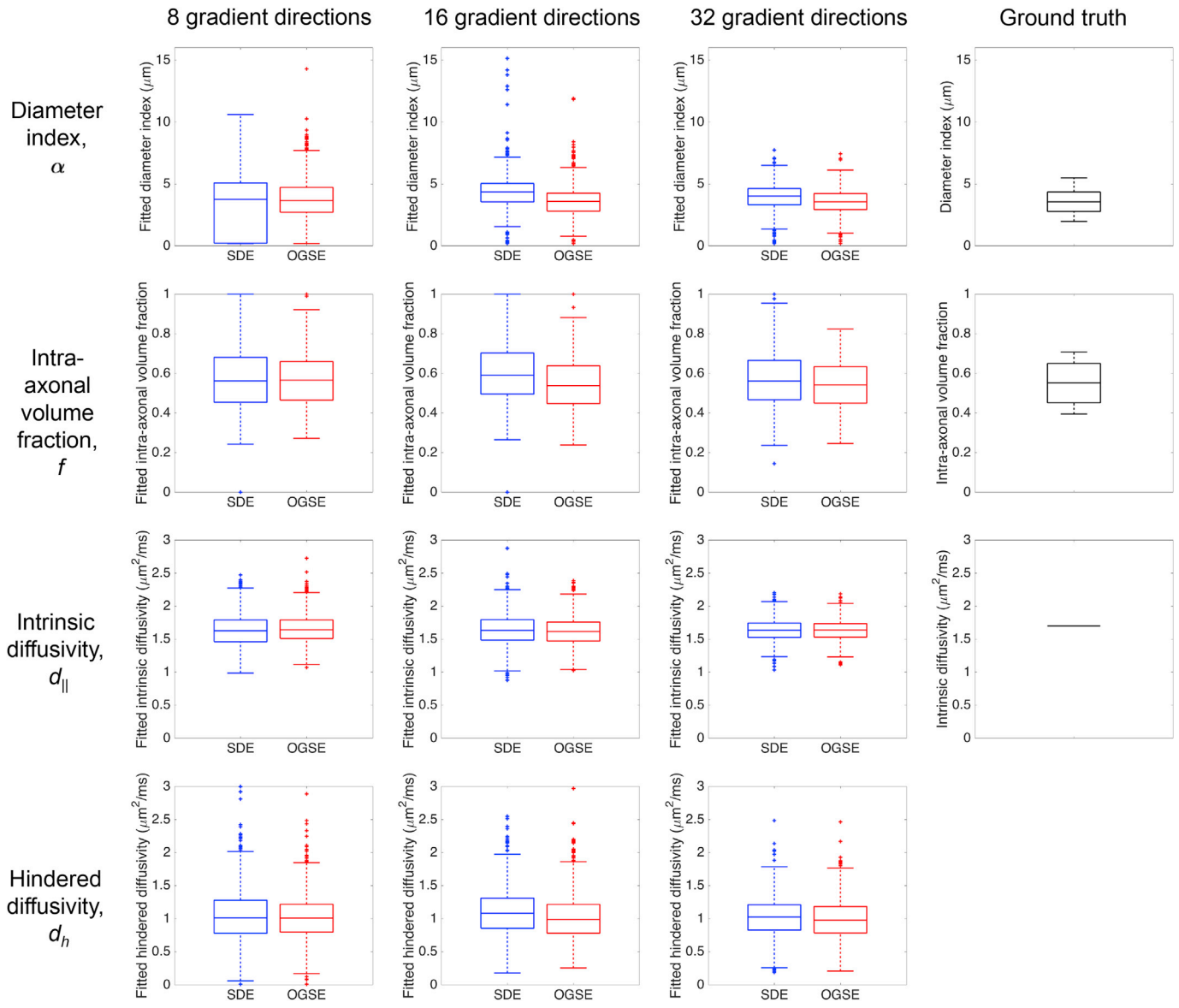

Fig. 8. Robustness of estimated parameters with respect to the number of gradient directions. Box-whisker plots of the median estimates for each substrates across its 50 instances of added noise (SNR = 10). All twenty-eight substrates are included and the results plotted for SDE (in blue) and OGSE (in red) protocols. The ground truth model parameters of each substrates are also plotted on the far right panel (except for d_h for which the value is unknown). The boxes show median, 25th and 75th percentiles of the uncertainty and the whiskers extend to the most extreme data points excluding outliers.

conditions, that low-frequency OGSE may improve accuracy of axon diameter mapping compared to using the standard SDE protocol.

The work shows that the imaging results match the simulation results reasonably well. The signal attenuation in the experimental data is 10–20% higher than in simulations, as can be seen from the signal curves in Figs. 5 and 11. This is likely due to the higher intrinsic diffusivity in the tissue compared to that used in the simulations. However, the model estimates and the trends in the comparison between the OGSE and the SDE protocols are approximately the same between the two experiments. Furthermore, the signal in the free diffusion direction at high b-values in tissue cannot be distinguished from the noise floor, as seen in (Fig. 11) and matches that in simulations (Fig. 5). This is very similar to *in vivo* studies (Alexander et al., 2010) in which the effect of "stationary water" (observed as constant non-zero signal in the free diffusion direction), that is usually present in fixed tissue and modelled as an extra compartment (Panagiotaki et al., 2010; Stanisz et al., 1997), is not present and suggests that our tissue is in as close to *in vivo* condition as possible.

The results we obtain here support the theoretical results recently published in Drobnjak et al. (2016) and Nilsson et al. (2017). They showed that when gradients are perfectly perpendicular to the fibres, SDE provides maximum sensitivity to axon diameter, while OGSE sequences have slightly lower performance. However, as the angle departs from the perfect 90°, SDE sensitivity drastically drops, and OGSE becomes more beneficial than SDE. The main reason for this is that as the angular deviation grows, the signal contribution from free diffusion parallel to the fibres and hence sequences with high b-values (such as the optimal SDE sequences) significantly attenuate the signal and reduce the sensitivity. OGSE sequences have an order of magnitude lower b-value and hence better preserve the parallel signal and the overall sensitivity. This effect is present when there is fibre orientation dispersion, as well as when using HARDI acquisition for perfectly parallel fibres with unknown orientation. The lower the number of directions in the HARDI acquisition, the larger the average angular deviation from perpendicular, and hence the more advantageous OGSE is expected to be. Furthermore, during protocol optimisation, as the number of gradient directions is reduced from 32 to 8, the optimisation enforces both SDE and OGSE to

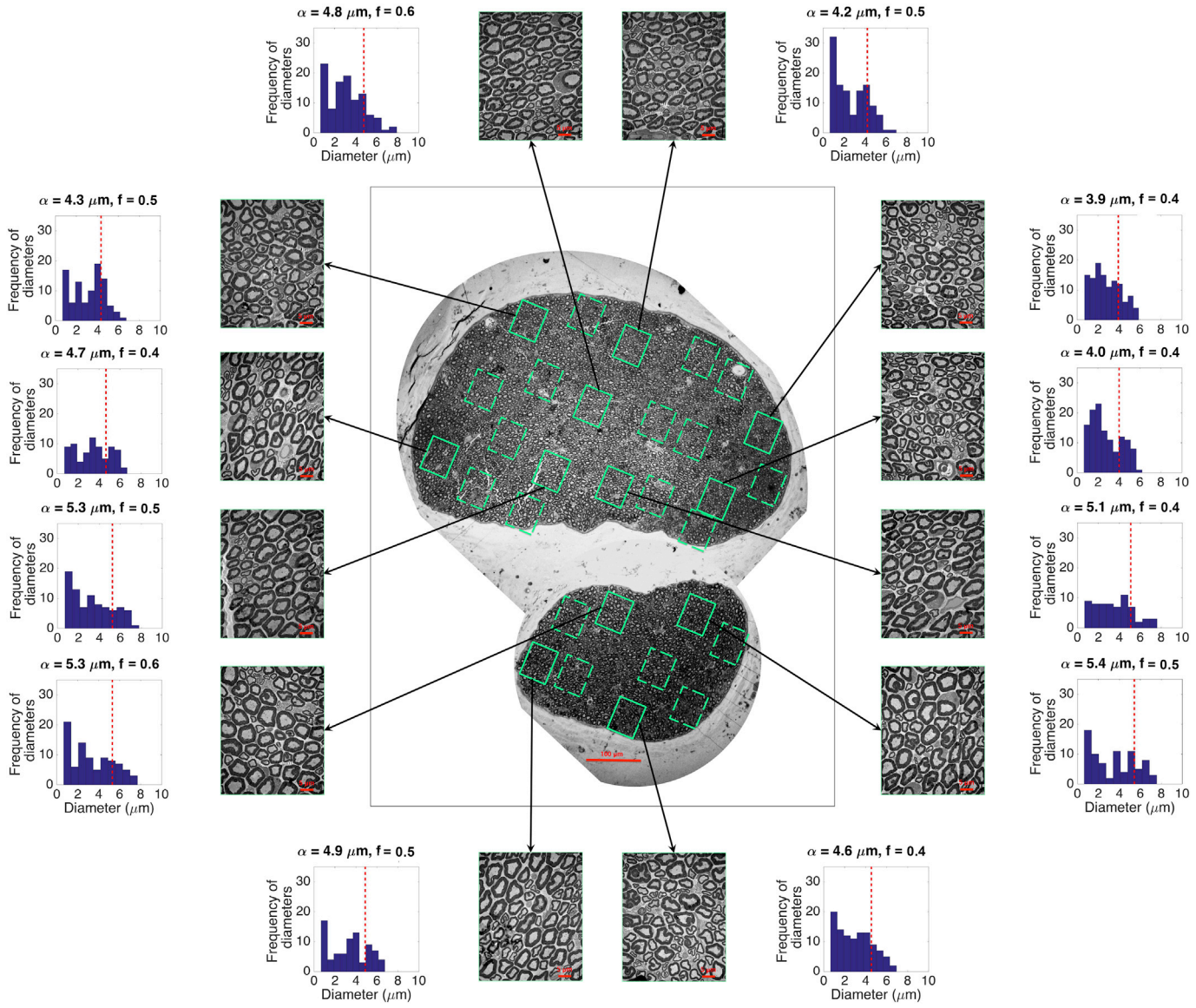

Fig. 9. TEM image of the entire nerve tissue section taken from the nerve in the middle of the MR volume, with a scale bar = 100 μm. Thirty high magnification TEM images of the axons at the indicated positions within the nerve fascicles are also acquired, two of which are excluded due to artefacts. 12 examples of the magnified TEM images and their corresponding histograms of their axon diameter distributions (corrected for the 30% tissue shrinkage) are shown. The red bars on the high magnification TEM image indicate the scale bar = 5 μm. The axon diameter index α for a given ROI is indicated as a red dashed line and the corresponding intra-axonal volume fraction is labelled on each histogram.

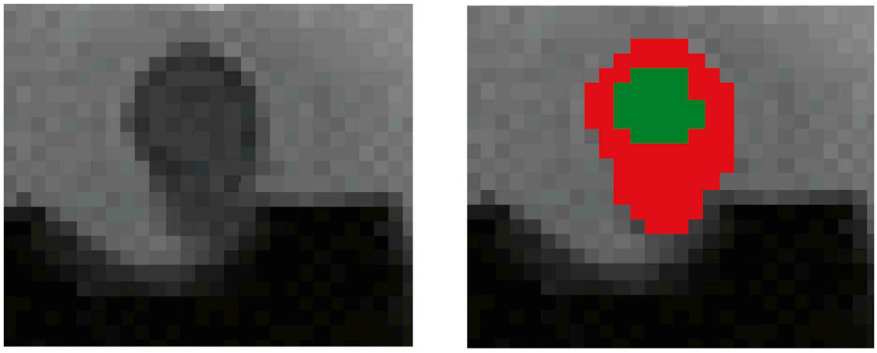

Fig. 10. (a) A T_2 weighted cross-sectional image of the nerve with no diffusion weighting applied. The black shape at the bottom of the image is the platform which the nerve is resting on. (b) Region of interest selected for the analysis. The red region covers the whole cross-sectional section of the nerve drawn on top of the b = 0 image shown in (a). The green region is a selected subsection of the red region, fully within the upper fascicle, used for quantitative analysis.

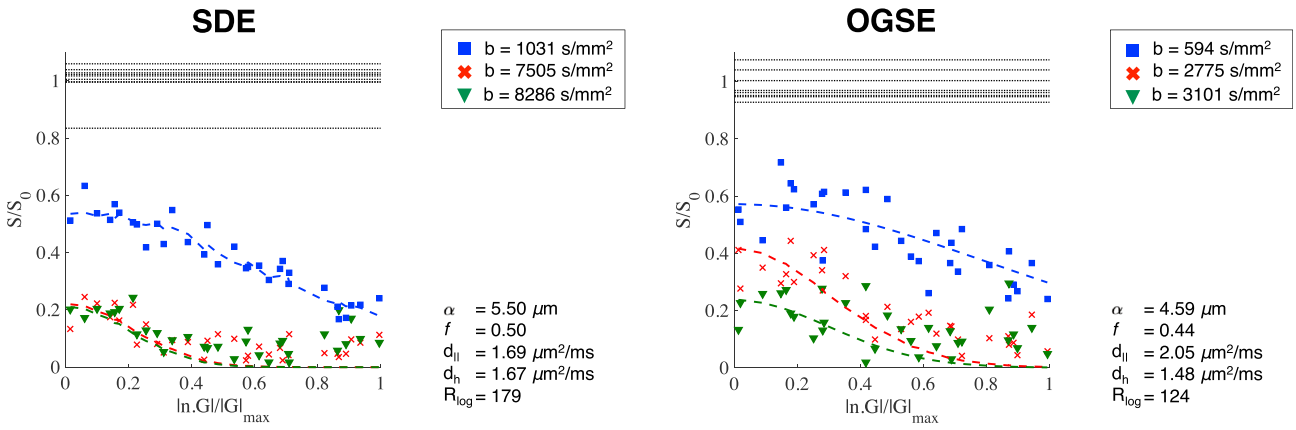

Fig. 11. Graphs showing the model signals fitted (dashed lines) to the experimental data (data points) for an example voxel from the 32 gradient directions SDE (left) and OGSE (right) protocols. The same explanation of the plots as in Fig. 5 applies. The horizontal dashed lines around $S/S_0 = 1$ represent the 9 normalised non-diffusion weighted measurements and their variation corresponds to the underlying noise in the data.

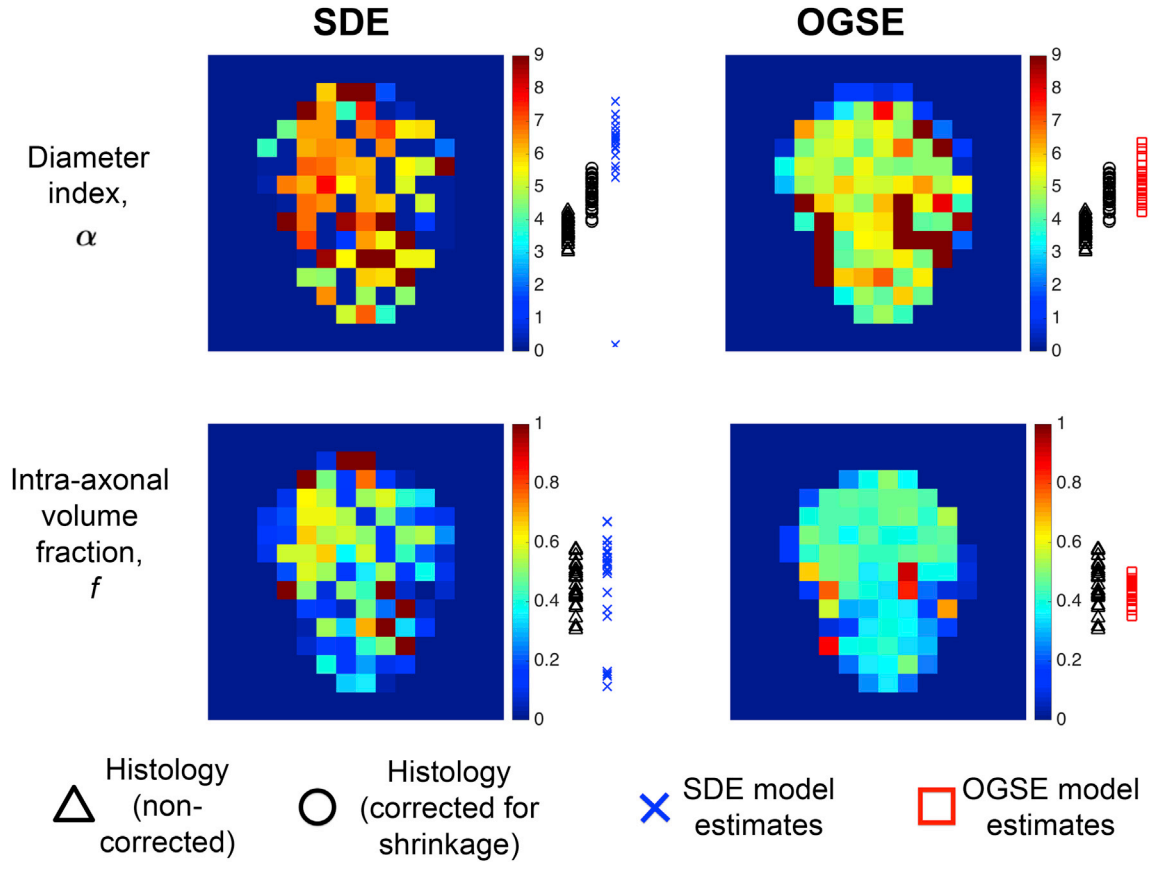

Fig. 12. Accuracy of estimated parameters in the viable nerve experiment using the 32 direction SDE (left) and OGSE (right) protocols. Maps show the estimates for each individual voxel in the red ROI defined in Fig. 10b. Blue crosses and red squares show the estimates from the green ROI for SDE and OGSE protocol respectively. Black circles are parameter estimates from the twenty-eight histology regions (corrected for 30% tissue shrinkage), and black triangles are the non-corrected axon diameter estimates from the same regions. Axonal diameter indices in the colour bar are in μm.

reduce b-values in order to minimise the signal loss due to the parallel gradient component, and consequently both protocols have reduced durations of the long pulses in the optimised sequences.

It is notable that in every optimised SDE protocol two of the selected shells are nearly identical. This result has also been observed previously in Alexander et al. (2010) and suggests that, for the given model, no alternative SDE waveforms are needed to further enrich the information provided. OGSE waveforms by comparison, with their extra parameter (ω) can have more variable forms and tend to be optimised by a combination of three different complementary waveforms. As the model complexity increases both SDE and OGSE may exhibit a larger variety of different waveforms.

In this study we chose to use OGSE sine profiles. This contrasts with other studies which have used cosine profiles in order to sample "purely" the diffusion spectra in the temporal diffusion spectroscopy models (Does et al., 2003). In our approach however we directly fit the model of the tissue into the measured data, without sampling the spectra first, so any gradient waveform will give accurate estimates of the model parameters,

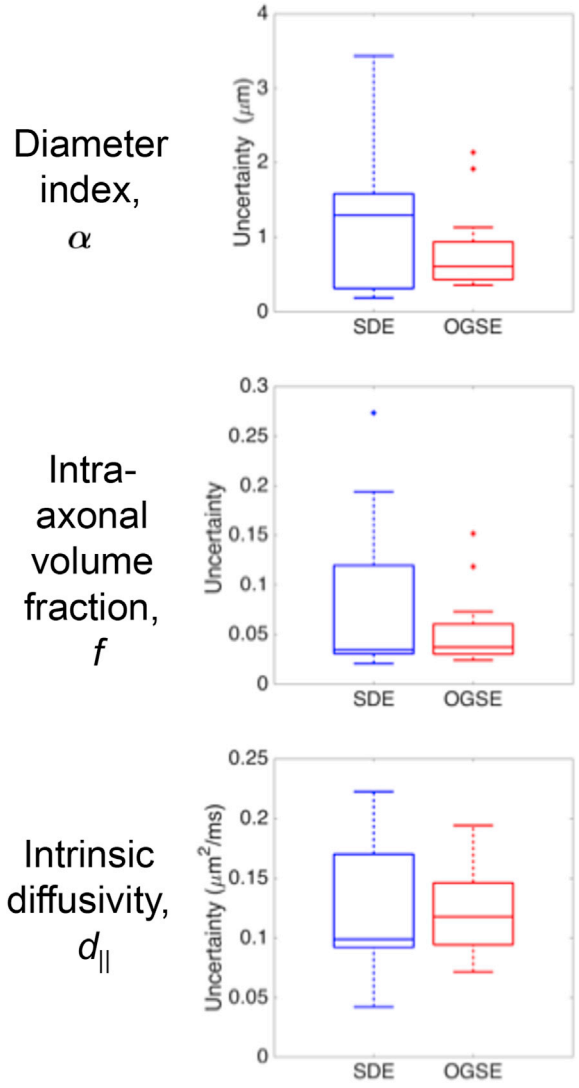

Fig. 13. Precision of estimated parameters in viable nerve experiment using the 32 direction SDE (in blue) and OGSE (in red) protocols. Box-whisker plots of the uncertainty calculated as the standard deviation of the posterior distribution are shown. The boxes show median, 25th and 75th percentiles of the uncertainty and the whiskers extend to the most extreme data points excluding the outliers.

conditional on the accuracy of the biophysical model. There has been recent results (Ianus et al., 2016), which suggest that cosine waveforms have a slightly higher sensitivity towards the axon diameter and we will be looking into this in the future.

We used a specialised viable tissue chamber introduced in Richardson et al. (2013), and were hence able to do a long 12 h scanning session. Richardson et al. (2013) demonstrated that changes in microstructure within the nerve in that period are minimal. We also carefully tested our experimental set-up using a separate set of sciatic nerve (left and right nerve), one fixed immediately after the extraction and the other immersed in aCSF, scanned for 12 h and then fixed. We found that axon sizes, shapes and myelin sheath are similar for both nerves.

4.1. Limitations

In this work we choose a simple model of white matter tissue. Specifically, the model uses long straight circular cylinders that mimic axon bundles and does not account for curvature of axons, dispersion or crossing fibres. Since the nerves in our tissue sample have been ligated then attached to the platform in a manner that maintained their natural tension within the chamber (as in Fig. 1), we believe the effects of this simplification are minimised. Whilst it has been shown that axons can demonstrate an 'undulating' course through certain peripheral nerves (which would indeed manifest as an effective orientation dispersion in a diffusion MR signal), it has also been demonstrated that a small amount of tension on the nerve can straighten the axons and remove these undulations. This effect is discussed in Pourmand et al. (1994) and Nilsson et al. (2012). However, we understand this is a simple scenario and in the future we will improve the set up of the viable tissue (i.e. to account for undulation and dispersion) to explore the performance of OGSE and SDE protocols experimentally under realistic conditions. Similar to the results here, we expect OGSE protocols to perform better than SDE protocols as has been theoretically demonstrated by Drobnjak et al. (2016) and Nilsson et al. (2017).

It can also be noted that many of the axons seen in the histology slides are quite eccentric in shape, as observed in other histology studies (Petit et al., 2014), which deviates from the circular cylindrical geometry assumed by the model (similar to models used by Assaf and Basser (2005) and Alexander et al. (2010)). We expect that the random orientation of these geometric deviations from a perfect cylinder across the large population of axons could potentially average out, and consequently the effect of eccentricity on the analysis should be small.

Another assumption of the model is that there is no signal contribution from the myelin. In reality, myelin water contributes partially to the signal. However, based on the standard T_2 values for myelin (Assaf et al., 2002; Webb et al., 2003) and echo time in our protocols, we find that the contribution is only up to 4–5%, which given our low SNR of around 15 would not contribute meaningfully to the signal. Our model also assumes Gaussian diffusion to describe the collective contribution of extra-axonal water from microstructure, including glial cells and blood vessels, and although this is a well established method (Alexander et al., 2010; Assaf et al., 2004; Santis et al., 2016; Xu et al., 2014), it might not be the most accurate assumption and we plan to investigate it further in the future.

Additionally, although our model estimates d_h, which in itself is more realistic than using the simple tortuosity assumption, the model does not assume that d_h is time dependent. Time dependence of d_h has been previously reported in Burcaw et al. (2015) and Santis et al. (2016) and we investigated the effect it has on our data (see Supplementary Material 4). We used Monte Carlo simulations and looked at the extra-axonal space in isolation and found that for the substrates and the diffusion times we used here the effect is not statistically significant. Finally, we assume that the intra- and extra-axonal intrinsic diffusivity is the same and it has been suggested that they could be different in tissue (Jelescu et al., 2015). However, as pointed out in Ferizi et al. (2014), this particular assumption of separate diffusivities mainly affects our model results if dispersion occurs in tissue, which we do not expect to see in our tissue as the nerve is taut.

Furthermore, Monte Carlo simulations have been performed assuming a Gamma distribution of axon diameters, however, histology based estimates are noisy and can exhibit departures from the theoretical distribution. While we do not expect this to have a significant impact on the results, future work aims to account for more realistic distributions to better capture the variations shown in histology. Finally, we use a shrinkage factor of 30% and assume that all compartments shrink equally, which might not be perfectly accurate. Tissue shrinkage can vary between 10% and 40% (Innocenti et al., 2014b) and although our procedure is similar and 30% is widely accepted (Innocenti et al., 2014a), it is extremely difficult to validate it for individual samples. Hence, we also show the uncorrected histology values of axon diameter in Figs. 12 and 14 and find that these are approximately 40% lower than OGSE and 70% lower than SDE estimates, suggesting that the OGSE estimates are within the accepted shrinkage variation, while SDE are much larger than that.

The model used in optimisation is slightly different to the model used during fitting, as it assumes the tortuosity constraint in the extracellular space. Although it would have made more sense to use the same model for fitting, our model selection revealed that the tortuosity constraint

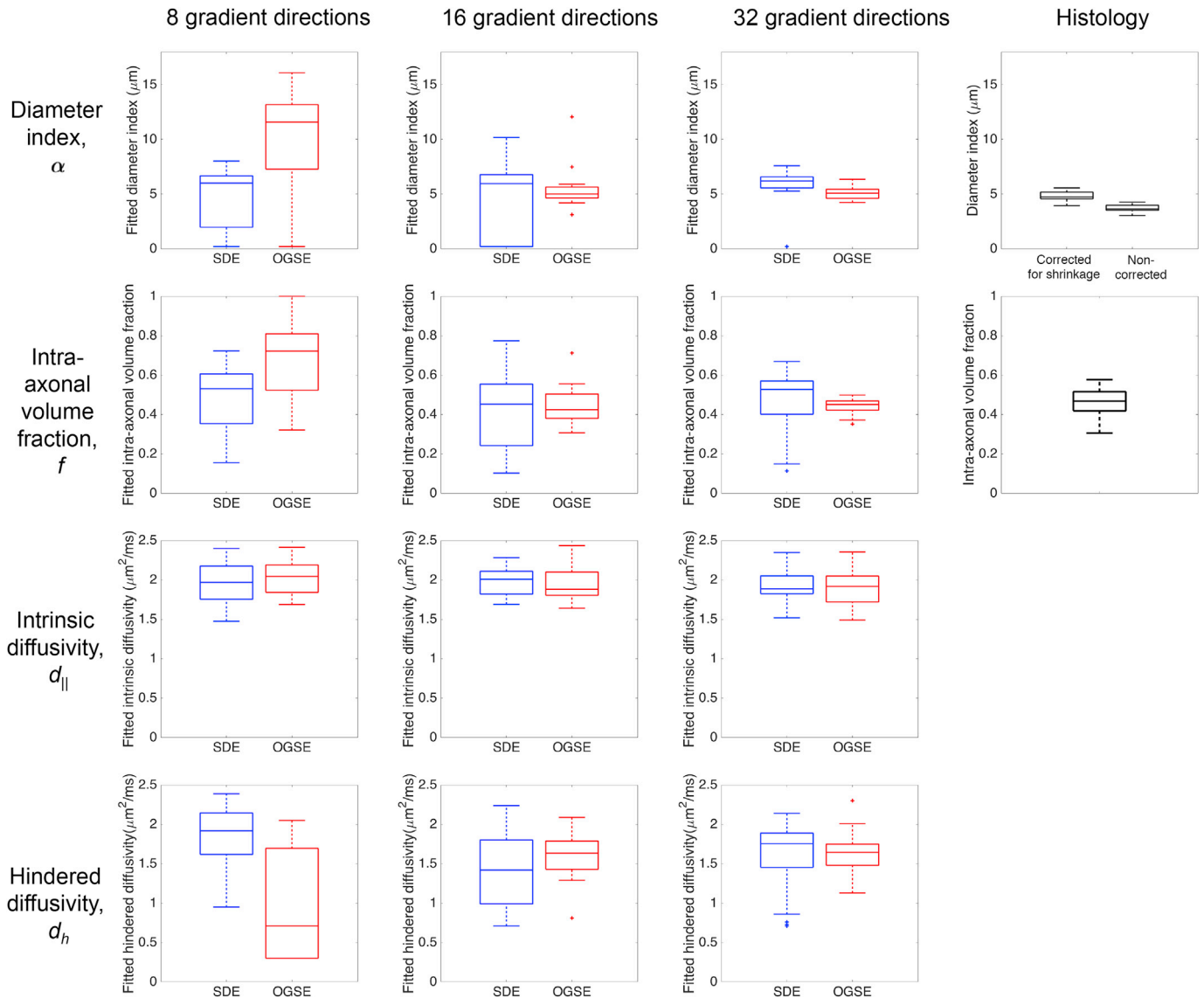

Fig. 14. Robustness of estimated parameters in viable nerve experiments with respect to the number of gradient directions. The figure shows box-whisker plots of the parameter estimates within the green ROI in Fig. 10b of the nerve obtained for SDE (blue) and OGSE (red) protocols. Axon diameters estimated from histology are plotted on the far right panel, corrected for shrinkage on the left and non-corrected on the right. Volume fractions estimated from histology are also given. The boxes show median, 25th and 75th percentiles of the uncertainty with respect to the noise and the whiskers extend to the most extreme data points excluding the outliers.

biases the diameter and intra-axonal volume fraction estimates (similar to Burcaw et al. (2015)), and hence we relaxed this constraint, which significantly improved the fitting. Similarly as in Alexander et al. (2010), we do not expect that using this slightly different model during optimisation would change our conclusions. Furthermore, the model parameters used to optimise the protocols were not the same as the values determined here from the histology of the nerve tissue. We tested this in simulation and found that using histology values for the optimisation gives sequences with slightly lower b-value and more variation within protocols, however no statistical difference in the parameter estimates.

The experiments were done for only one gradient strength of G = 800 mT/m. Previous work has demonstrated that the gradient strength dependence is strong, and as the strength reduces the sensitivity to axon diameter decreases as indeed shown in Sepehrband et al. (2016). Further sensitivity study carried out in simulations and theoretically by Drobnjak et al. (2016) and Nilsson et al. (2017) for a range of gradient strengths found that OGSE wins over SDE in all cases. We hence, extrapolate that we would expect to see similar results experimentally.

Estimates of hindered diffusivity in nerve tissue have a relatively high level of uncertainty, higher than estimates from the simulations. Simulations benefit from ground truth substrate parameters that inform hindered diffusivity estimation (as described in Methods), however it is possible that the tissue data does not support sufficiently the fitting method we used, especially for cases with less data such as the 8 gradient directions protocol, and a more complex fitting procedure is needed.

4.2. Extrapolation to clinical systems

Low frequency OGSE sequences are safe and easy to implement and use on standard clinical scanners (Baron and Beaulieu, 2014; Kakkar et al., 2017; Van et al., 2014) and do not cause peripheral nerve stimulation. The key limitation is the inherent lack of sensitivity to axon diameter at clinical gradient strengths. For gradients of 60–80 mT/m and standard SNR of 20, the resolution limit is approximately 5 μm (Drobnjak et al., 2016; Nilsson et al., 2017) and hence, brain imaging is a real challenge since the majority of axon diameters in the brain are smaller than 3 μm (Aboitiz et al., 1992) and are unrecoverable with either SDE or OGSE sequences. On the other hand, axon diameters in the peripheral

nervous system are larger, 3–14 μm (Jacobs and Love, 1985; Schroder et al., 1988), and here the clinical transition is a realistic possibility. Furthermore, more powerful clinical scanners such as the Connectome with 300 mT/m and higher SNR reduces the resolution limit to 2–3 μm, which could make clinical imaging possible in the brain as well (as demonstrated by McNab et al. (2013), Huang et al. (2015) and Ferizi et al. (2015)).

With the continuing improvements in the SNR of scanners and the rise in clinical gradient strengths, the number of potential clinical applications of axon diameter imaging is likely to increase in the future. Here, the use of OGSE protocols will be essential for maximising the potential of such techniques as we work to develop them further and ultimately translate them into clinical use.

Acknowledgements

This work was funded by: EPSRC (EP/K502959/1, EP/J500331/1), the EPSRC-funded UCL Centre for Doctoral Training in Medical Imaging (EP/L016478/1) and the NIHR-funded Biomedical Research Centre at University College London Hospitals. The study was undertaken at Centre for Advanced Biomedical Imaging (CABI) and University College London (UCL), both of whom are part-funded by the Department of Health NIHR Biomedical Research Centres funding scheme.

Appendix A. Supplementary data

Supplementary data related to this article can be found at http://dx.doi.org/10.1016/j.neuroimage.2017.07.060.

References

Aboitiz, F., Scheibel, A.B., Fisher, R.S., Zaidel, E., 1992. Fiber composition of the human corpus callosum. Brain Res. 598, 143–153.
Alexander, D.C., 2008. A general framework for experiment design in diffusion MRI and its application in measuring direct tissue-microstructure features. Magn. Reson. Med. 60, 439–448.
Alexander, D.C., Hubbard, P.L., Hall, M.G., Moore, E.A., Ptito, M., Parker, G.J., Dyrby, T.B., 2010. Orientationally invariant indices of axon diameter and density from diffusion MRI. NeuroImage 52, 1374–1389.
Assaf, Y., Basser, P.J., 2005. Composite hindered and restricted model of diffusion (CHARMED) mr imaging of the human brain. Neuroimage 27, 48–58.
Assaf, Y., Blumenfeld-Katzir, T., Yovel, Y., Basser, P.J., 2008. AxCaliber: a method for measuring axon diameter distribution from diffusion MRI. Magn. Reson. Med. 59, 1347–1354.
Assaf, Y., Freidlin, R.Z., Rohde, G.K., Basser, P.J., 2004. New modeling and experimental framework to characterize hindered and restricted water diffusion in brain white matter. Magn. Reson. Med. 52, 965–978.
Assaf, Y., Kafri, M., Shinar, H., Chapman, J., Korczyn, A.D., Navon, G., Cohen, Y., 2002. Changes in axonal morphology in experimental autoimmune neuritis as studied by high b-value q-space ^{1}h and ^{2}h dqf diffusion magnetic resonance spectroscopy. Magn. Reson. Med. 48, 71–81.
Baron, C.A., Beaulieu, C., 2014. Oscillating gradient spin-echo (OGSE) diffusion tensor imaging of the human brain. Magn. Reson. Med. 72, 726–736.
Basser, P.J., Mattiello, J., LeBihan, D., 1994. MR diffusion tensor spectroscopy and imaging. Biophys. J. 66, 259–267.
Benjamini, D., Komlosh, M.E., Holtzclaw, L.A., Nevo, U., Basser, P.J., 2016. White matter microstructure from nonparametric axon diameter distribution mapping. NeuroImage 135, 333–344.
Burcaw, L.M., Fieremans, E., Novikov, D.S., 2015. Mesoscopic structure of neuronal tracts from time-dependent diffusion. NeuroImage 114, 18–37.
Burke, D., 2007. The properties of axons differ according to their function. J. Physiol. 578, 1–2.
Callaghan, P.T., 2011. Translational Dynamics and Magnetic Resonance: Prin- Ciples of Pulsed Gradient Spin Echo NMR, 1 ed. Oxford University Press.
Cluskey, S., Ramsden, D.B., 2001. Mechanisms of neurodegeneration in amyotrophic lateral sclerosis. Mol. Pathol. 54, 386.
Cook, P.A., Bai, Y., Nedjati-Gilani, S., Seunarine, K.K., Hall, M.G., Parker, G.J., Alexander, D.C., 2006. Camino: open-source diffusion-mri reconstruction and processing. In: ISMRM Annual Meeting, P. 2759. ISMRM Abstract.
Devroye, 1986. Non-uniform Random Variate Generation. Springer-Verlag NewYork Inc.
Does, M.D., Parsons, E.C., Gore, J.C., 2003. Oscillating gradient measurements of water diffusion in normal and globally ischemic rat brain. Magn. Reson. Med. 49, 206–215.
Dortch, R.D., Harkins, K.D., Juttukonda, M.R., Gore, J.C., Does, M.D., 2013. Characterizing inter-compartmental water exchange in myelinated tissue using relaxation exchange spectroscopy. Magn. Reson. Med. 70, 1450–1459.
Drobnjak, I., Alexander, D.C., 2011. Optimising time-varying gradient orientation for microstructure sensitivity in diffusion-weighted MR. J. Magn. Reson. 212, 344–354.
Drobnjak, I., Siow, B., Alexander, D.C., 2010. Optimizing gradient waveforms for microstructure sensitivity in diffusion-weighted MR. J. Magn. Reson. 206, 41–51.
Drobnjak, I., Zhang, H., Ianus, A., Kaden, E., Alexander, D.C., 2016. PGSE, OGSE, and sensitivity to axon diameter in diffusion MRI: insight from a simulation study. Magn. Reson. Med. 75, 688–700.
Dyrby, T.B., Soggard, L.V., Hall, M.G., Ptito, M., Alexander, D.C., 2013. Contrast and stability of the axon diameter index from microstructure imaging with diffusion MRI. Magn. Reson. Med. 70, 711–721.
Ferizi, U., Schneider, T., Panagiotaki, E., Nedjati-Gilani, G., Zhang, H., Wheeler-Kingshott, C.A.M., Alexander, D.C., 2014. A ranking of diffusion MRI compartment models with in vivo. Magn. Reson. Med. 72, 1785–1792.
Ferizi, U., Schneider, T., Witzel, T., Wald, L.L., Zhang, H., Wheeler-Kingshott, C.A.M., Alexander, D.C., 2015. White matter compartment models for in vivo diffusion dMRI at 300 mt/m. NeuroImage 118, 468–483.
Hall, M.G., Alexander, D.C., 2009. Convergence and parameter choice for monte-carlo simulations of diffusion MRI. IEEE Trans. Med. Imaging 28, 1354–1364.
Holz, M., Heila, S.R., Saccob, A., 2000. Temperature-dependent self-diffusion coefficients of water and six selected molecular liquids for calibration in accurate 1H NMR PFG measurements. Phys. Chem. Chem. Phys. 2, 4740–4742.
Home Office, 2000. Animals (Scientific Procedures) Act 1986: Guidance on the Operation of the Animals (Scientific Procedures) Act 1986. HC (Series) (Great Britain. Parliament. House of Commons), Stationery Office.
Huang, S.Y., Nummenmaa, A., Witzel, T., Duval, T., Cohen-Adad, J., Wald, L.L., McNab, J.A., 2015. The impact of gradient strength on in vivo diffusion mri estimates of axon diameter. NeuroImage 106, 464–472.
Hursh, J.B., 1939. Conduction velocity and diameter of nerve fibers. Am. J. Physiol. 127, 131–139.
Ianus, A., Shemesh, N., Alexander, D.C., Drobnjak, I., 2016. Double oscillating diffusion encoding and sensitivity to microscopic anisotropy, 00, 00–00.
Ikeda, M., Oka, Y., 2012. The relationship between nerve conduction velocity and fiber morphology during peripheral nerve regeneration. Brain Behav. 2, 382–390.
Innocenti, G.M., Caminiti, R., Aboitiz, F., 2014a. Comments on the paper by horowitz et al. Brain Struct. Funct. 220, 1789–1780.
Innocenti, G.M., Vercelli, A., Caminiti, R., 2014b. The diameter of cortical axons depends both on the area of origin and target. Cereb. Cortex 24, 2178–2188.
Jacobs, J.M., Love, S., 1985. Qualitative and quantitative morphology of human rural nerve at different ages, 108.
Jelescu, I.O., Veraart, J., Adisetiyo, V., Milla, S.S., Novikov, D.S., Fieremans, E., 2015. One diffusion acquisition and different white matter models: how does microstructure change in human early development based on WMTI and NODDI? NeuroImage 107, 242–256.
Jespersen, S.N., 2012. Equivalence of double and single wave vector diffusion contrast at low diffusion weighting. NMR Biomed. 25, 813–818.
Jiang, X., Li, H., Xie, J., Zhao, P., Gore, J.C., Xu, J., 2016. Quantification of cell size using temporal diffusion spectroscopy. Magn. Reson. Med. 75, 1076–1085.
Kakkar, L.S., Atkinson, D., Chan, R.W., Siow, B., Ianus, A., Drobnjak, I., 2017. Sensitivity of OGSE ActiveAx to Microstructural Dimensions on a Clinical Scanner. Springer International Publishing, pp. 85–97.
Kempton, L.B., Gonzalez, M.H., Leven, R.M., Hughes, W.F., Beddow, S., Santhiraj, Y., Archibald, S.J., Hassan, B.E., Shott, S., Kerns, J.M., 2009. Assessment of axonal growth into collagen nerve guides containing vegf-transfected stem cells in matrigel. Anat. Rec. 29, 214–224.
Komlosh, M.E., Özarslan, E., Lizak, M.J., Horkay, F., Schram, V., Shemesh, N., Cohen, Y., Basser, P.J., 2011. Pore diameter mapping using double pulsed-eld gradient mri and its validation using a novel glass capillary array phantom. J. Magn. Reson. 208, 128–135.
Li, H., Gore, J.C., Xu, J., 2014. Fast and robust measurement of microstructural dimensions using temporal diffusion spectroscopy. J. Magn. Reson. 242, 4–9.
Mattiello, J., Basser, P., LeBihan, D., 1994. Analytical expressions for the b matrix in NMR diffusion imaging and spectroscopy. J. Magn. Reson. 108, 131–141.
McNab, J.A., Edlow, B.L., Witzel, T., Huang, S.Y., Bhat, H., Heberlein, K., Feiweier, T., Liu, K., Keil, B., Cohen-Adad, J., Tisdall, M.D., Folkerth, R.D., Kinney, H.C., Wald, L.L., 2013. The human connectome project and beyond: initial applications of 300 mt/m gradients. NeuroImage 80, 234–245.
Mercredi, M., Vincent, T.J., PBidinosti, C., Martin, M., 2016. Assessing the accuracy of using oscillating gradient spin echo sequences with axcaliber to infer micron-sized axon diameters. Magn. Reson. Mater. Phys. Biol. Med. 1–14.
Nedjati-Gilani, G.L., Schneider, T., Hall, M.G., Cawley, N., Hill, I., Ciccarelli, O., Drobnjak, I., Wheeler-Kingshott, C.A.M.G., Alexander, D.C., 2017. Machine learning based compartment models with permeability for white matter microstructure imaging. NeuroImage 150, 119–135.
Nilsson, M., Lasic, S., Drobnjak, I., Topgaard, D., Westin, C.F., 2017. Resolution limit of cylinder diameter estimation by diffusion MRI: the impact of gradient waveform and orientation dispersion. NMR Biomed., e3711 n/a.
Nilsson, M., Ltt, J., Sthlberg, F., Westen, D.V., Hagsltt, H., 2012. The importance of axonal undulation in diffusion MR measurements: a monte carlo simulation study. NMR Biomed. 25, 795–805.
Nilsson, M., Westen, D.V., Sthlberg, F., Sundgren, P.C., Hagsltt, H., Ltt, J., 2013. The role of tissue microstructure and water exchange in biophysical modelling of diffusion in white matter. MAGMA 26, 345–370.
Ong, H.H., Wehrli, F.W., 2010. Quantifying axon diameter and intra-cellular volume fraction in excised mouse spinal cord with q-space imaging. Neuroimage 51, 1360–1366.
Panagiotaki, E., Hall, M.G., Zhang, H., Siow, B., Lythgoe, M.F., Alexander, D.C., 2010. High-fidelity meshes from tissue samples for diffusion MRI simulations. In: Medical

Image Computing and Computer-assisted Intervention, MICCAI 2010, Lecture Notes in Computer Science 6362/2010, pp. 404–411.
Parsons, E.C., Does, M.D., Gore, J.C., 2006. Temporal diffusion spectroscopy: theory and implementation in restricted systems using oscillating gradients. Magn. Reson. Med. 55, 75–84.
Petit, B., Giraudet, F., Bchon, C., Bardin, L., Avan, P., Boespflug-Tanguy, O., Bgou, M., 2014. Mice with a deletion of the major central myelin protein exhibit hypersensitivity to noxious thermal stimuli: involvement of central sensitization. Neurobiol. Dis. 65, 55–68.
Piven, J., Bailey, J., Ranson, B.J., Arndt, S., 1997. An MRI study of the corpus callosum in autism. Am. J. Psychiatry 154, 1051.
Pourmand, R., Ochs, S., Jersild, R.A., 1994. The relation of the beading of myelinated nerve fibers to the bands of fontana. Neuroscience 61, 373–380.
Reynaud, O., Winters, K.V., Hoang, D.M., Wadghiri, Y.Z., Novikov, D.S., Kim, S.G., 2016. Surface-to-volume ratio mapping of tumor microstructure using oscillating gradient diffusion weighted imaging. Magn. Reson. Med. 76, 237–247.
Richardson, S., Siow, B., Batchelor, A.M., Lythgoe, M.F., Alexander, D.C., 2013. A viable isolated tissue system: a tool for detailed mr measurements and controlled perturbation in physiologically stable tissue. Magn. Reson. Med. 69, 1603–1610.
Ritchie, J.M., 1982. On the relation between fibre diameter and conduction velocity in myelinated nerve fibres. Proc. RRoy. Soc. Lond. Ser. B, Biol. Sci. 217, 29–35.
Sanders, F.K., 1948. The thickness of the myelin sheaths of normal and regenerating peripheral nerve fibres. Proc. RRoy. Soc. Lond. Ser. B, Biol. Sci. 135, 323–357.
Santis, S.D., Jones, D.K., Roebroeck, A., 2016. Including diffusion time dependence in the extra-axonal space improves in vivo estimates of axonal diameter and density in human white matter. NeuroImage 130, 91–103.
Sasaki, S., Maruyama, S., 1992. Increase in diameter of the axonal initial segment is an early change in amyotrophic lateral sclerosis. J. Neurol. Sci. 110, 114–120.
Schroder, J.M., Bohl, J., Brodda, K., 1988. Changes of the ratio between myelin thickness and axon diameter in the human developing sural nerve. J. Neurol. Sci. 76, 114–120.
Sepehrband, F., Alexander, D.C., Clark, K.A., Kurniawan, N.D., Yang, Z., Reutens, D.C., 2016. Parametric probability distribution functions for axon diameters of corpus callosum. Front. Neuroanat. 10, 59.
Shemesh, N., Alvarez, G.A., Frydman, L., 2015. Size distribution imaging by non-uniform oscillating-gradient spin echo (NOGSE) MRI. PLoS One 10, 1–19.
Siow, B., Drobnjak, I., Chatterjee, A., Lythgoe, M.F., Alexander, D.C., 2012. Estimation of pore size in a microstructure phantom using the optimised gradient waveform diffusion weighted nmr sequence. J. Magn. Reson. 214, 51–60.
Siow, B., Drobnjak, I., Ianus, A., Christie, I.N., Lythgoe, M.F., Alexander, D.C., 2013. Axon radius estimation with oscillating gradient spin echo (ogse) diffusion MRI. diffusion-fundamentals.Org. 18, 1–6.
Stanisz, G.J., Szafer, A., Wright, G.A., Henkelman, R.M., 1997. An analytical model of restricted diffusion in bovine optic nerve. Magn. Reson. Med. 37, 103–111.
Szafer, A., Zhong, J., Gore, J.C., 1995. Theoretical model for water diffusion in tissues. Magn. Reson. Med. 33, 697–712.
Van, A.T., Holdsworth, S.J., Bammer, R., 2014. In vivo investigation of restricted diffusion in the human brain with optimized oscillating diffusion gradient encoding. Magn. Reson. Med. 71, 83–94.
Webb, S., Munro, C.A., Midha, R., Stanisz, G.J., 2003. Is multicomponent t2 a good measure of myelin content in peripheral nerve? Magn. Reson. Med. 49, 638–645.
Xu, J., Li, H., Harkins, K.D., Jiang, X., Xie, J., Kang, H., Does, M.D., Gore, J.C., 2014. Mapping mean axon diameter and axonal volume fraction by MRI using temporal diffusion spectroscopy. NeuroImage 103, 10–19.
Zikopoulos, B., Barbas, H., 2010. Changes in prefrontal axons may disrupt the network in autism. J. Neurosci. 30, 14595–14609.